Anisotropic and heterogeneous thermal conductivity in programmed liquid metal composites through direct ink writing

Ohnyoung Hur[1], Eric J. Markvicka[3,4,5*], and Michael D. Bartlett[1,2*]

[1]Mechanical Engineering, Soft Materials and Structures Lab, Virginia Tech, Blacksburg, VA 24061, USA.
[2]Macromolecules Innovation Institute, Virginia Tech, Blacksburg, VA 24061, USA.
[3]Mechanical & Materials Engineering, Smart Materials & Robotics Lab, University of Nebraska–Lincoln, Lincoln, NE 68588
[4]Electrical & Computer Engineering, University of Nebraska–Lincoln, Lincoln, NE 68588
[5]School of Computing, University of Nebraska–Lincoln, Lincoln, NE 68588

*To whom correspondence should be addressed: eric.markvicka@unl.edu, mbartlett@vt.edu

Cite this article: Hur, O., Markvicka, E.J., and Bartlett, M. D., "Anisotropic and heterogeneous thermal conductivity in programmed liquid metal composites through direct ink writing." *Advanced Functional Materials* 35.11 (2025): 2417375.

Abstract

Thermal management in electric vehicles, electronics, and robotics requires the systematic ability to dissipate and direct the flow of heat. Thermally conductive soft composites are promising for thermal management due to their high thermal conductivity and mechanical flexibility. However, composites typically have the same microstructure throughout a film, which limits directional and spatial control of thermal management in emerging systems that have distributed heat loads. Herein, directional and spatially tunable thermal properties are programmed into liquid metal (LM) soft composites through a direct ink writing (DIW) process. Through the local control of LM droplet aspect ratio and orientation this programmable LM microstructure has a thermal conductivity in the direction of LM elongation of 9.9 W/m·K, which is ∼40 times higher than the unfilled elastomer (0.24 W/m·K). The DIW process enables LM droplets to be oriented in specific directions with tunable aspect ratios at different locations throughout a continuous film. This introduces anisotropic and heterogeneous thermal conductivity in compliant films to control the direction and magnitude of heat transfer. This methodology and resulting materials can provide designed thermal management solutions for rigid and soft devices.

Keywords: direct ink writing, liquid metal, anisotropy, heterogeneous, thermal conductivity

Introduction

Thermal management in electric vehicles, robotics, and soft electronics is critical, especially with the increasing incorporation of artificial intelligence into these systems.[1–3] To address this challenge, the need for efficient spatial and directional thermal management has become increasingly important.[4,5] Thermal interface materials, which are typically composed of a compliant polymer matrix with thermally conductive rigid inclusions, play a critical role in heat transfer.[6,7] However, the random dispersion of inclusions often results in isotropic behavior.[8,9] One approach to achieve directional thermal control in these soft composites is through controlled microstructures with unidirectionally aligned inclusions.[10,11] This has been achieved through mechanical,[12,13] magnetic,[14,15] and chemical[16] alignment of solid particles. While these approaches improve anisotropic thermal conductivity, incorporating solid particles into a polymer matrix often reduces flexibility, which is important for thermal management.[17] Additionally, this method only provides unidirectional heat control, limiting its ability to manage heat spatially.

Gallium-based liquid metal (LM) has recently been adopted as a thermally conductive inclusion due to its high thermal conductivity and mechanical flexibility.[18–23] In addition to these properties, LM shows multifunctional properties such as reconfigurability,[24] low viscosity,[25] and low toxicity.[26] These unique attributes have led to the integration of LM soft composites (LMSCs) in various fields, including soft electronics [27–33], soft robotics,[34–36] stretchable sensors [37–42], and thermal management applications.[43–45] To fabricate LMSCs, high-shear mixing is a common method for dispersing LMs within elastomers, which results in randomly distributed spherical LM particles and therefore requires additional process steps to program microstructure.[43,46,47] LM droplets can be processed into elongated microstructrues for enhanced thermal conductivity through techniques such as mechanical deformation,[20,48] magnetic alignment,[49–51] or annealing processes.[43,52] However, these approaches require external forces or pre-/post-treatment during or after curing the LM composite to

achieve stable microstructures, resulting in uniform (i.e. homogeneous) structures throughout the film, which limits multidirectional heat dissipation control. Alternatively, material extrusion additive manufacturing techniques can program material properties on demand during the printing process.[53–58] For example, direct ink writing (DIW) has been used to create LM microstructures with spherical to elongated inclusions throughout a film without pre-/post-processing or external forces.[42,59–61] By tuning material and printing parameters, this fabrication methodology offers the opportunity for advanced thermal management where properties like thermal conductivity can be programmed during the printing process.

Here, LMSC films with local control of LM microstructure including droplet aspect ratio, orientation, and direction are created through a DIW process for spatially tunable and directional thermal conductivity. This approach creates LM microstructures including spherical and elongated LM droplets throughout a film (Figure 1a). By utilizing elongated LM droplets, LMSCs with a high anisotropic thermal conductivity of 9.9 W/m·K are achieved, approximately 40× higher than the unfilled elastomer (Figure 1b), while maintaining mechanical flexibility (Figure 1c). By tuning the DIW print path, anisotropic and heterogeneous LM microstructures are programmed at different locations within a film to tune thermal conductivity as a function of position (Figure 1d,e), which enables control of the direction and magnitude of heat transfer across a plane. This control over heat transfer can be observed through infrared (IR) imaging of a high power LED on a film, where the heat dissipation is directional, preferentially transferring the heat generated to a prescribed location (left side) of the film (Figure 1f; Video S1, Supporting Information). This method, which enables tunable and selective heat dissipation by controlling LM microstructures, offers a versatile thermal management solution for applications in thermal diodes, soft electronics, and soft robotics.

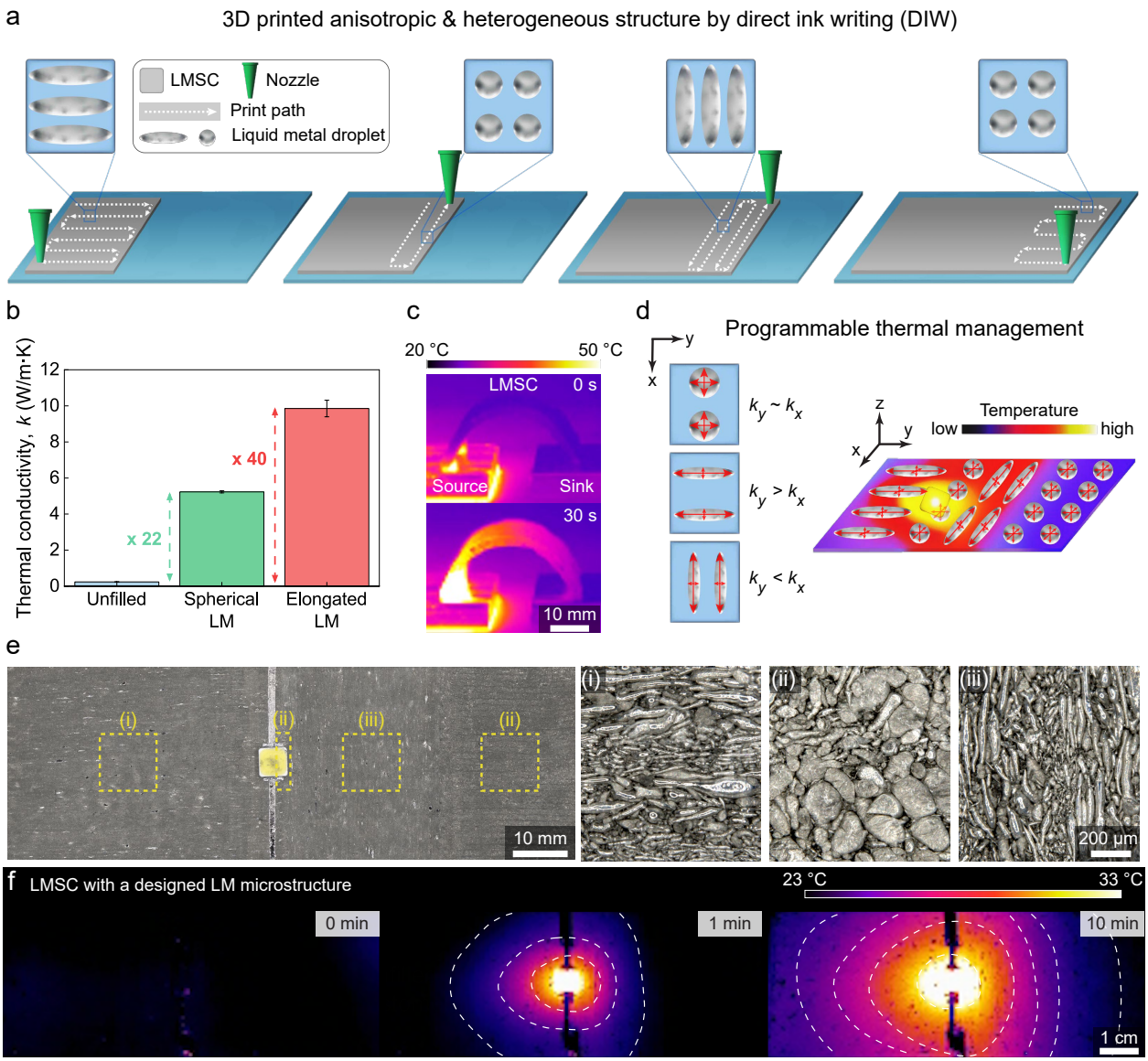

Fig. 1 Programmable thermal conductivity by designing LM microstructure through DIW printing. a) Schematic of the DIW printing process to design anisotropic and heterogeneous LM microstructure. The LM droplet schematic shows a top view image. **b)** Thermal conductivity of three different samples. **c)** IR images show the flexibility and heat dissipation performance of LMSC with elongated LM. **d)** Left schematic shows that isotropic/anisotropic thermal conductivity of the LM microstructure. Right schematic shows the anticipated thermal dissipation in the directed path with designed LM microstructures (the yellow square is an LED). **e)** Optical micrograph of a DIW printed LMSC that includes three different regions. (i) Horizontally elongated LM microstructure. (ii) Spherical LM microstructure. (iii) Vertically elongated LM microstructure. **f)** IR image with a time sequence of the LMSC with designed microstructures as shown in *e*. The dashed line shows the boundary of different temperature regimes.

Results and Discussion

Isotropic thermal conductivity

The thermal conductivity of LM composites is highly dependent on the volume fraction of LM (ϕ, where ϕ = volume of LM / volume of LM and elastomer), the microstructure of the LM (spherical or elongated), and the orientation of the LM (random or aligned). Here, LMSC with different ϕ (0 to 80% with an increase of 10%) were fabricated by a casting. The effect of ϕ on the isotropic thermal conductivity ($k_{isotropy}$) of LMSC with a randomly distributed spherical LM microstructure was measured with a modified transient plane source (MTPS, Figure 2a). The unfilled elastomer ($\phi = 0\%$, pristine ExSil) shows a thermal conductivity of 0.24 W/m·K, whereas the LMSC with $\phi = 80\%$ shows 5.23 W/m·K, a 22× increase over the unfilled elastomer. The measured thermal conductivity as a function of ϕ agrees well with the Bruggeman effective medium theory (EMT) theory (red dashed line in Figure 2a).[62]

To investigate the effect of droplet size on thermal conductivity, high volume fraction LMSC (ϕ = 60, 70, 80%) were selected. Particle size is then modified by utilizing hexane during the high-shear mixing process to reduce the viscosity of the emulsion during the initial LM droplet formation as the emulsion's viscosity affects droplet size.[46,60,63] The hexane is removed before casting the samples by placing the uncured emulsion into a vacuum chamber for 1.5 hours before casting. Hereafter, we define W/Hx as LMSC modified with hexane, and W/O Hx as unmodified LMSC. The change of LM droplet size (D) was observed through optical microscopy (Figure 2b) and was quantitatively measured through particle image analysis. The distribution of D for W/O Hx LMSC and W/ Hx LMSC are then fitted by a Gaussian distribution and the results are presented in Figure 2c and Figure S1. Adding hexane shifts the histogram to the right (increasing D) owing to the temporary decrease of viscosity during mixing. The mean D with a standard deviation, obtained from Gaussian fitting, increased from 84.1 to 228 μm for LMSC ($\phi = 60\%$) and 46 to 109 μm for LMSC (ϕ

= 80%), respectively (Figure 2d). This enables the ability to tune droplet size for a given volume loading.

The $k_{isotropy}$ of W/O Hx and W/ Hx LMSC were measured trough MTPS method (Figure 2e). As shown in Figure 2f, LMSC with a larger D (W/ Hx) showed a slightly higher $k_{isotropy}$ (less than 8%). From this result, controlling droplet size for a given ϕ has a minimal impact on thermal conductivity, so other approaches are needed to enhance thermal conductivity.

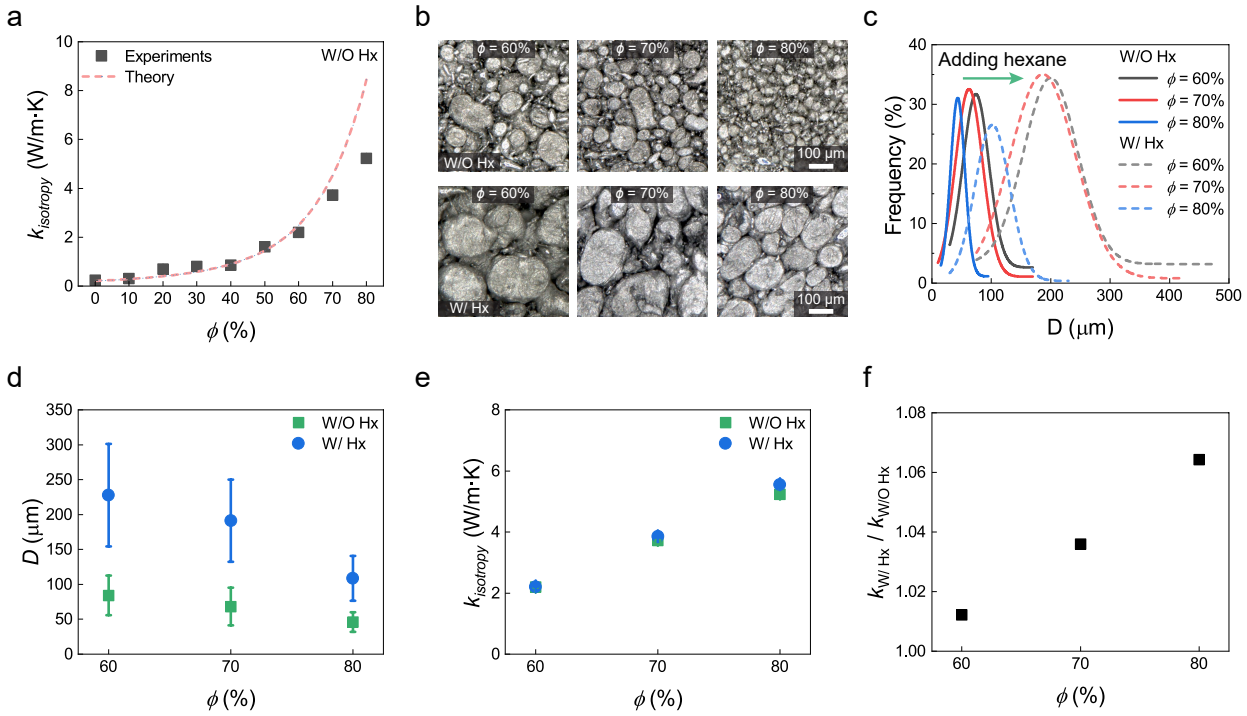

Fig. 2 Isotropic thermal conductivity ($k_{isotropy}$) **a)** $k_{isotropy}$ with different ϕ. ($n = 5$) The dashed line (red) is Bruggeman effective medium theory.[62] ($n = 100$) **b)** Microscope images of LM droplets unmodified by hexane (W/O Hx, small D) and modified by hexane (W/ Hx, large D) with different ϕ. **c)** Histogram of LM droplet size (D) of W/O Hx (solid line) and W/ Hx (dashed line) with different ϕ (60% , 70%, and 80%). **d)** D of different ϕ for W/O Hx (green) and W/ Hx (blue). Error bar is standard deviation ($n \sim 100$). **e)** $k_{isotropy}$ with different ϕ (60%, 70%, and 80%) for W/O Hx and W/ Hx LMSC. ($n = 5$). **f)** The $k_{isotropy}$ ratio between W/ Hx and W/O Hx LMSC with different ϕ (60%, 70%, and 80%). Data in a, d, e, and f are plotted as the mean ± s.d., if error bars are not visible the data symbol is larger than the error bars.

High anisotropic thermal conductivity achieved by designing LM microstructure with DIW printing

LM droplet shape is a key microstructural component for controlling thermal conductivity.[20,43] We utilize DIW to tune the LM droplet aspect ratio (AR, described in Figure 3a inset) by shaping LM droplets directly at the tip of the print nozzle during extrusion. Here, the relative velocity (V^*) between the extrusion rate (C) and print head speed (V) is defined as $V^* = V/C$ and is tuned to control droplet AR. We used $V^* = 2$ to print spherical LM microstructures and $V^* = 12$ to print elongated LM microstructures. This creates homogeneous samples where the LM microstructure is elongated in one direction, where we define the thermal conductivity in the direction of printing as k_y and the thermal conductivity perpendicular to this direction in plane as k_x and out plane as k_z. We focus on three high LM-loading LMSC (ϕ = 60%, 70%, and 80%) with different droplet size (W/O Hx or W/ Hx) with two different printing conditions ($V^* = 2$ and 12).

To evaluate the AR of LMs in LMSC, at least 100 particles were analyzed and plotted with a box chart (Figure S2). The mean value from the box chart of AR is presented in Figure 3a-c. AR of LMs in LMSC increased with a higher V^* and a larger D (W/ Hx). Changes (more elongated LM microstructures) in LM microstructures of LMSC with increased V^* and modification by hexane are presented through optical microscopy images in Figure 3d. Here, we observe that AR increases with increasing V^* and D (i.e. W/ Hx).

To investigate the anisotropic thermal conductivity (k_y or $k_{x=z}$) of the LMSC, a transient hot wire (THW) method was adopted (Figure 3e). k_{axial} represents the measured thermal conductivity when the platinum (Pt) wire is placed parallel to the alignment of the elongated LMs, while $k_{transverse}$ represents the measured thermal conductivity when Pt wire is placed perpendicular to the orientation of ellipsoidal LMs (Figure 3e). The measured k_{axial} and $k_{transverse}$ for LMSCs are presented in Figure S3. These values can be transformed for the calculation of orthotropic bulk properties represented by (k_x, k_y, k_z).[20,64,65] With this trans-

formation, the relationship between anisotropic thermal conductivity and the orientation of elongated LMs can be determined.

Through this analysis method, $k_{x=z}$ is measured and the data are presented with different ϕ in Figure 3f. We find that $k_{x=z}$ increases with ϕ, due to the higher concentration of LM. Furthermore, regardless of the use of hexane or through different printing condition, $k_{x=z}$ was similar for each volume loading as the heat transfer path perpendicular to the elongation droplets was not significantly changed. However, the anistoropic thermal conductivity in the direction of elongation (k_y) shows marked changes with different LM microstructures (Figure 3g). When LMSC has more elongated and aligned LM microstructure (W/ Hx, V^* = 12, green), it shows higher k_y than LMSC with spherical microstructure (W/O Hx, V^* = 2, black) and LMSC with slightly elongated microstructures (W/O Hx, V^* = 12, blue) even though the LMSC includes the same ϕ. Furthermore, W/ Hx, V^* = 12, ϕ = 70% shows similar k_y as W/ Hx, V^* = 12, ϕ = 80%, which we attribute to more elongated LM droplets in the ϕ = 70% sample compared with the ϕ = 80% sample (Figure S4). As shown in Figure 3h, LMSC (ϕ = 70%) showed the highest enhancement in k_y (84%) relative to the same volume loading but with less elongated droplets (W/O Hx, V^* = 12). This is because LMSC (ϕ = 70%, V^* = 12) showed the largest increase (about 88%) in mean AR from 2.32 (W/O Hx, V^* = 12) to 4.37 (W/ Hx, V^* = 12). LSMC (ϕ = 70%, W/ Hx, V^* = 12 shows elongated LM microstructure throughout the entire sample (Figure S5). Therefore, we choose the W/ Hx, V^* = 12, ϕ = 70%, LMSC composition and processing conditions for heat dissipation demonstration in Figure 4. These experiments demonstrate that DIW can effectively program LM microstructure to greatly enhance thermal conductivity. This results in as manufactured LM composites with high thermal conductivities of $k_y = 9.8 \pm 0.88$ W/m·K with LMSC (ϕ = 70 %) manufactured W/Hx and V^* = 12. This is approximately 40 times higher than unfilled elastomer, and represents an exceptional combination of high compliance and high thermal conductivity for an as manufactured soft composite.

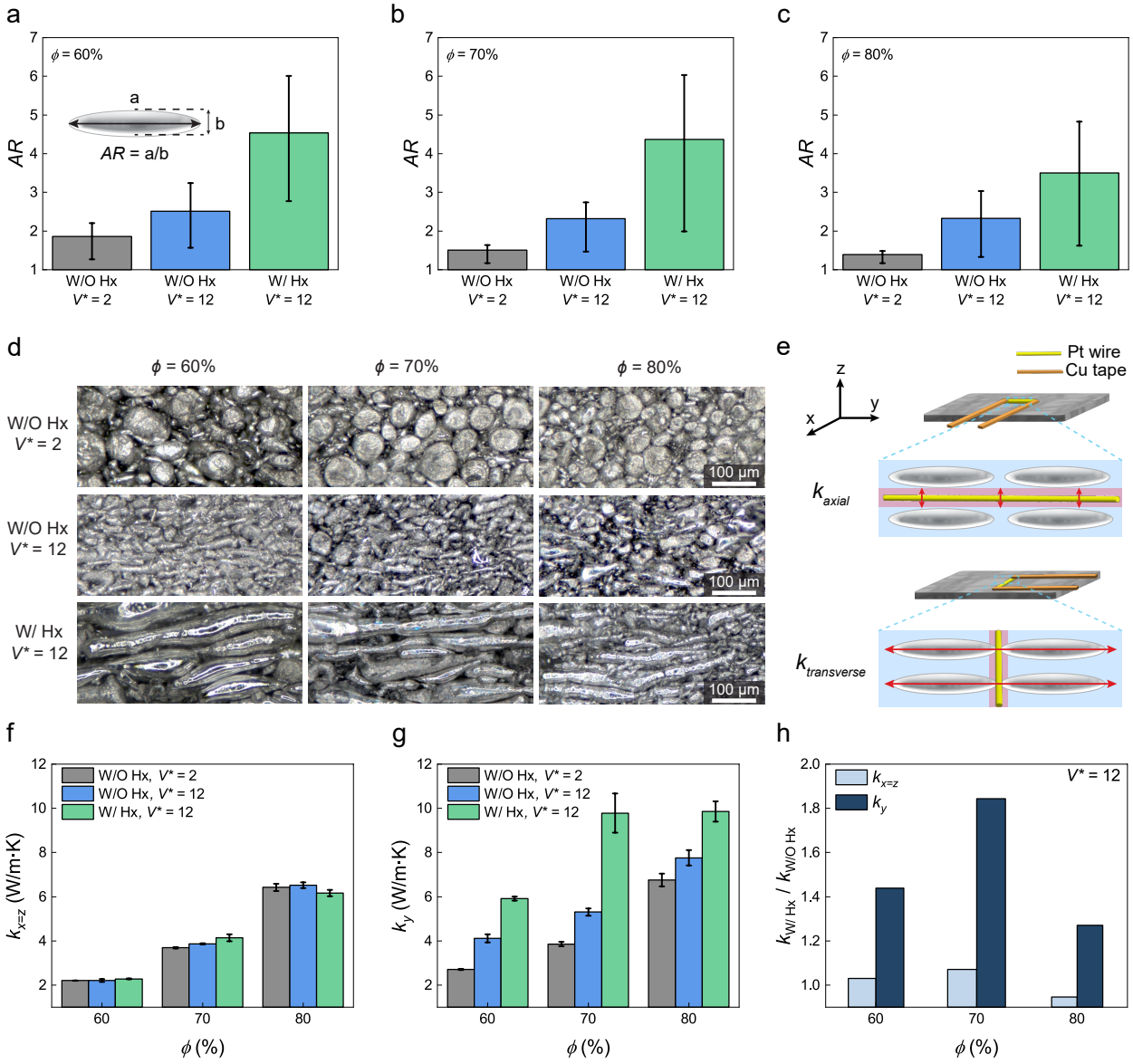

Fig. 3 Anisotropic thermal conductivity of DIW printed LMSC. Aspect ratio (AR) for different ϕ, D (W/O Hx or W/ Hx), and printing conditions ($V^* = 2$ or 12) **a)** $\phi = 60\%$, **b)** $\phi = 70\%$, and **c)** $\phi = 80\%$. Upper error bar is $Q3$ and lower error bar is $Q1$ from the box plot (See the details in Figure S2). **d)** Microscope images of LMSC presented in *a-c*. **e)** A schematic showing the measurement of anisotropic thermal conductivity (k_{axial} and $k_{transverse}$) to get k_x, k_y, and k_z. Anisotropic thermal conductivity for **f)** $k_{x=z}$ and **g)** for k_y with different ϕ (60% to 80%). **h)** The ratio of anisotropic thermal conductivity between small D (W/O Hx) and large D (W/ Hx) for different ϕ.

Controllable heat dissipation path with designed LM microstructure through DIW

Through the DIW process, we can create highly elongated microstructures throughout soft films by tuning the process conditions. We can orient the LM droplets in different directions on demand by controlling the print path, while also using materials that enable stretchability and flexibility as shown in Figure S6. This provides a unique opportunity to create soft thermal films that have prescribed anisotropic and spatially varying properties for heterogeneous structures that control the direction and magnitude of heat conduction.

To demonstrate this capability, we designed an LMSC (W/ Hx, $\phi = 70\%$) with three distinct LM-microstructures regions. We define these as region (i), horizontally elongated LM droplets, region (ii), vertically elongated LM droplets, and region (iii), spherical LM droplets (Figure 4a). Microscope images show each region with programmed LM microstructures in Figure 4b. The LMSC with a designed structure still demonstrates mechanical flexibility, as shown in Figure 4c. To evaluate the microstucture control of heat dissipation, two different samples (unfilled elastomer and LMSC with the designed structure) were tested with a high power LED at room temperature (Figure 4d and Figure S7; Video S1, Supporting Information). The LED was placed in the same location for all samples on the right edge of region (i), as shown in Figure 4a and d. The same power (3.7V and 0.35A) was applied to the LED in all cases to turn on the LED at the beginning. As shown in Figure 4d and e, the heat dissipation from the LED is different between each sample (unfilled elastomer and LMSC (designed)). For example, the unfilled elastomer showed heat accumulation around the LED as it has a low thermal conductivity (0.24 W/m·K) which resulted in poor heat conduction and dissipation that resulted a damage in the LED (a top inset in Figure 4e). However, the LMSC with designed inclusions showed better heat conduction and dissipation properties without any damage on LED (a bottom inset in Figure 4e) as they have high thermal conductivity. In addition, the LMSC with a designed structure exhibited directed

heat conduction along a desired pathway. Here the LM inclusions in region (i) are oriented in y axis, which results in enhanced y-directional thermal conductivity relative to region (ii) where the LM inclusions are aligned to x axis. This creates an ellipsoidal thermal distribution in region (i), where heat is preferentially transferred along the y-axis due to the programmed elongated microstructures. However, a radial-like thermal distribution occurs within an unfilled elastomer and a LMSC with random (spherical LM microstructure) in regions (ii) and (iii) (see 60 seconds (s), 600 s IR images in Figure 4d and Figure S8). When the LED was turned off, the cooling property was also improved in the LMSC sample compared with the unfilled sample (Figure 4e).

To quantitatively evaluate the anisotropic heat dissipation performance, temperature changes at a different location in each sample are plotted in Figures 4f-h. As shown in Figure 4f, the LMSC with a designed structure showed a higher temperature than unfilled elastomer at almost regions (at distance $> \sim 10$ mm) due to its greater thermal conductivity. Furthermore, compared with the unfilled elastomer which has isotropic heat dissipation properties, LMSC with a designed structure showed higher temperatures in the left region than in the right, as it possesses anisotropic heat dissipation properties. This is attributed to the designed heat transfer path toward the left, facilitated by the elongated LM microstructure in that direction. For 600 s after turning on the LED, the LMSC with a designed structure exhibited higher anisotropic heat dissipation performance (a larger temperature gap between the left and right regions), while the unfilled elastomer showed continuous isotropic heat dissipation properties (Figure 4g). Additionally, the LMSC with a designed structure exhibited better cooling properties at all locations compared with the unfilled elastomer after turning off the LED, due to its high thermal conductivity (Figure 4h). These results demonstrate that by designing the LM microstructure, effective anistoropic heat dissipation can be achieved.

The ability to print a range of LM droplet microstructures–ranging from homogeneous to heterogeneous–using a single ink and manufacturing system enables the creation of soft

elastomer composites with tailored, anisotropic and heterogeneous thermal conductivity and heat transfer characteristics. This enables the control of heat flow within soft composite materials, towards preventing the thermal degradation of sensitive parts or electronic components to enhance their lifespan.

Conclusion

This work demonstrates LMSC with anisotropic and heterogeneous LM microstructures for thermal management systems with spatial and local heat control. These microstructures are achieved through a DIW process where they are directly manufactured and no pre-/post-processing are required to maintain or design LM microstructures. Controlling the LM droplet microstructure is performed directly at the print nozzle tip, which is attributed to the unique ability of the LM droplets to transform during the DIW process. By combining the control of LM inclusion elongation and the ability of high volume loading of inclusions, a highly anisotropic thermal conductivity of 9.9 ± 0.46 W/m·K is achieved, which is approximately $40\times$ higher than the unfilled elastomer. By leveraging this material system within the DIW process, we presented the ability to locally design LM microstructural features such as aspect ratio and orientation. This overcomes challenges in previous processing techniques where LM microstructure is either spherical or show a uniform (i.e. homogeneous) microstructure across the sample. This capability opens new avenues to design thermal management by programming different thermal capabilities within a film through a single process and a single ink. We anticipate that this will provide insight into soft materials for directional heat transfer that can be used to control thermal dissipation in emerging device architectures.

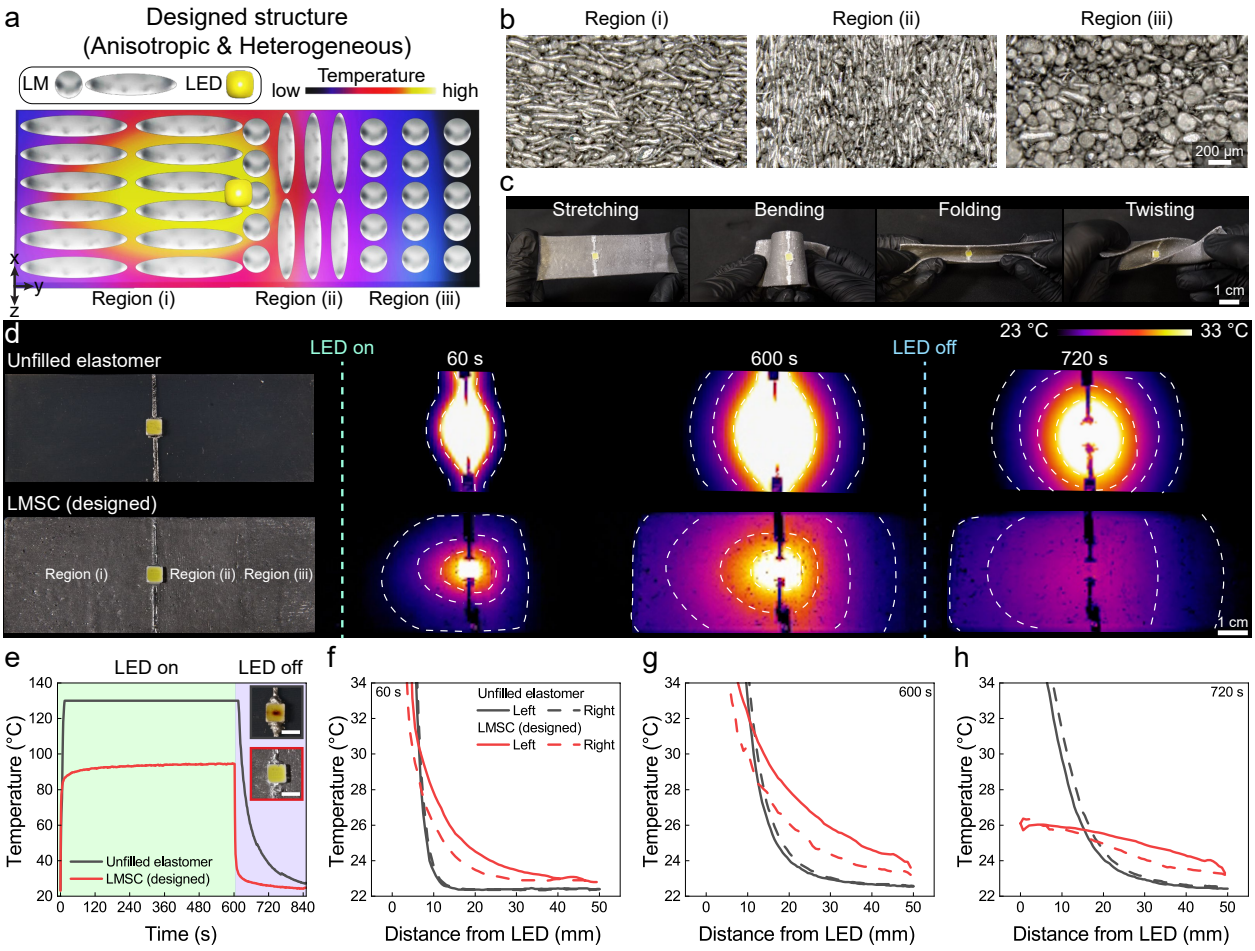

Fig. 4 Controllable heat dissipation with designed LM microstructure. **a)** Schematic for a designed LM microstructure with three different microstructures, region (i), region (ii), and region (iii). The color map shows the anticipated heat dissipation with the designed microstructures. **b)** Microscope images for three different regions in the designed LM structure. **c)** Images show mechanical flexibility of LMSC (designed). **d)** Optical images (left) and IR images (right) of heat dissipation test of two different samples, unfilled elastomer and LMSC with designed LM microstructures. **e)** The temperature (°C) changes with time (s) of each samples at LED. Inset images showed LEDs after 600 s operation (top: unfilled elastomer, bottom: LMSC (designed)). Scale bars are 3 mm. Temperature (°C) changes with a distance (mm) from LED: after **f)** 60 s and **g)** 600 s with the LED on. **h)** After 120 s with the LED off. The solid lines represent the temperature measurement at the left region of the LED, while the dashed lines represent the temperature measurement at the right region of the LED. *g* and *h* follow legend in *f*.

Experimental Section

Materials and Ink Fabrication: Eutectic gallium indium (EGaIn) was fabricated by mixing In:Ga in a weight ratio of 1:3, homogenized on a hot plate at 200 °C overnight. LM inks

were prepared through a two-step process. Initially, the ink was manually mixed using a glass rod. Subsequently, to achieve uniform dispersion of LM droplets in ExSil 100 (Gelest Inc.), a planetary centrifugal mixer (DAC 1200-500 VAC, FlackTek speed mixer) was employed. The mixing process was conducted at 800 rpm for 1 minute in a vacuum environment to remove air bubbles. For the fabrication of inks with large D LM droplets, hexane was added to the uncured ExSil in a 1:8 weight ratio and premixed before introducing LM. The LM was then dispersed using the FlackTek speed mixer under the same mixing conditions (800 rpm for 1 minute). Finally, the inks were placed in a vacuum chamber for 1.5 hours to eliminate any remaining hexane before the DIW printing process.

Casting Process: The mixed inks were poured into a clear acrylic plate with dimensions of 25 $\times$ 25 $\times$ 2 mm^3) and covered by a acrylic plate then gently pressed with clamps to create an even surface. Subsequently, the ink in the mold was cured in a convection oven at 80 °C overnight.

Fabrication of LMSC by DIW Process: The prepared ink was loaded into a syringe (BD 10mL syringe) with a tapered nozzle featuring an inner diameter of 0.84 mm. The syringe filled with LM inks was inserted into a material extrusion system (Hyrel SR 3D printer) equipped with an SDS-10 syringe head. Multilayer samples were then printed on sandpaper (600 Grit), with each sample having dimensions of 25 $\times$ 25 $\times$ 2 mm^3. The extrusion rate was set at 4.1 mm s^{-1} for both $V^* = 2$ and 12. The print head velocity was 8.1 and 49.2 mm s^{-1} for $V^* = 2$ and 12, respectively. To achieve the desired extrusion rate and print head velocity, we calculated these values based on the printed trace length and the syringe and nozzle inner diameters. The calculated values were then included in the G-code. The print height was 210 μm and 50 μm for $V^* = 2$ and 12, respectively. In the interval between printing each layer, a convection heating process using a 130 °C heat gun was applied for 3 minutes, followed by a cooling period using a cooling fan for 1 minute. Upon completing the multilayer printing, the printed samples were fully cured overnight in a convection oven set at 80 °C.

Optical Microscopy: Surface images of the printed samples were captured using an optical microscope (Zeiss Axiozoom v16 stereo-microscope). The morphology analysis of the LM droplets was conducted on the microscope images through Image J software. The outlines of the LM droplets were manually traced and converted into a binary image, distinguishing between elastomer and LM droplet areas. Subsequently, an ellipse fit was applied to each LM droplet section, for the extraction of major (a) and minor (b) axis length (inset images in Figure 3a). The major axis was considered the LM droplet size (D) for spherical droplets. The AR of the LM droplet was calculated by determining the ratio of the major to the minor axis of the fitted ellipse. To analyze the AR distribution of LM droplets in the printed structure, box plots were used (Figure S2).

Measurement of Thermal Conductivity: A C-Therm Trident model (MTPS method) was utilized to measure the isotropic thermal conductivity of the cast samples at room temperature.[66] The sample size was $25 \times 25 \times 2$ mm^3. The anisotropic thermal conductivity (k_{axial} and $k_{transverse}$) was determined using the THW method. From these values, k_y and $k_{x=z}$ were calculated as in previous work.[20] The sample size for this measurement was the same as that of the casting sample. This measurement process was repeated five times with 1-minute intervals to allow the sample to dissipate any residual heat from the previous test. The presented thermal conductivity is an average value from five different runs, along with a standard deviation.

LED Demonstration to Evaluate Designed Heat Dissipation Behaviors: To investigate the directed heat dissipation based on LM microstructure, two different samples were tested: unfilled and LMSC with designed structures. The unfilled sample was produced through a casting process. Unfilled ExSil was poured into a mold (dimensions: $100 \times 35 \times 2.5$ mm^3) and cured in an oven at 80 °C overnight. To fabricate LMSC with designed structures (Figure 4a), hexane was temporarily added to modify the LM ink ($\phi = 70\%$) viscosity to achieve a large D. All hexane was removed using a vacuum chamber for 1.5 hours before usage. The Hyrel 3D printer was adopted to print the designed structure, with the same

printing conditions as described in the fabrication of LMSC by DIW process section. For the region (i) and region (ii), V^* was set to 12, and a print height of 50 μm was utilized. For the region (iii) section, V^* was set to 2, and a print height of 210 μm was used. The region (i) section had dimensions of 50 $\times$ 35 mm^2, while the region (ii) and region (iii) sections had dimensions of 25 $\times$ 35 mm^2. The structure thickness was approximately 2.5 mm (50 layers for region (i) and region (ii), 12 layers for region (iii)). To assess the heat dissipation behavior, a LED (CreeLED, Inc.) was placed on the right edge of region (i) section for all samples. LM-Cu paste was utilized as electrodes to connect the LED to the power supply (RD6018, RIDEN). The LED was powered with a voltage of 3.7V and a current of 0.35A. An IR camera (E54sc, FLIR) recorded the heat dissipation properties with emissivity of 0.9 and reflection temperature = 20 °C. The LED was activated for 10 minutes, then turned off, and left for 5 minutes to evaluate the cooling properties. The limitation of the IR camera (the measurable maximum temperature is 130 °C) resulted in a temperature plateau in unfilled sample around 130 °C in Figure 4e.

Supporting Information

Supporting Information is available from the Wiley Online Library or from the author.

Acknowledgments

OH and MB acknowledge support through NSF (No. CMMI-2054409). EM acknowledges support through the NSF (No. CMMI-2054411).

Conflict of Interest

The authors declare that they have no known competing financial interests or personal relationships that could have appeared to influence the work reported in this paper.

Data Availability Statement

Data available on request from the authors.

Keywords

direct ink writing, liquid metal, anisotropy, heterogeneous, thermal conductivity

References

[1] Eren Sevinchan, Ibrahim Dincer, and Haoxiang Lang. A review on thermal management methods for robots. *Applied Thermal Engineering*, 140:799–813, 2018.

[2] Gilberto Moreno, Sreekant Narumanchi, Xuhui Feng, Paul Anschel, Steve Myers, and Phil Keller. Electric-drive vehicle power electronics thermal management: Current status, challenges, and future directions. *Journal of Electronic Packaging*, 144(1):011004, 2022.

[3] Hui Liu, AbdusSalam Aljbri, Jie Song, Jinqing Jiang, and Chun Hua. Research advances on ai-powered thermal management for data centers. *Tsinghua Science and Technology*, 27(2):303–314, 2021.

[4] Amol R Dhumal, Atul P Kulkarni, and Nitin H Ambhore. A comprehensive review on thermal management of electronic devices. *Journal of Engineering and Applied Science*, 70(1):140, 2023.

[5] Zhihao Zhang, Xuehui Wang, and Yuying Yan. A review of the state-of-the-art in electronic cooling. *e-Prime-Advances in Electrical Engineering, Electronics and Energy*, 1:100009, 2021.

[6] Junaid Khan, Syed Abdul Momin, and M Mariatti. A review on advanced carbon-based thermal interface materials for electronic devices. *Carbon*, 168:65–112, 2020.

[7] Yingyan Zhang, Jun Ma, Ning Wei, Jie Yang, and Qing-Xia Pei. Recent progress in the development of thermal interface materials: a review. *Physical Chemistry Chemical Physics*, 23(2):753–776, 2021.

[8] Mengmeng Qin, Yuxiao Xu, Rong Cao, Wei Feng, and Li Chen. Efficiently controlling the 3d thermal conductivity of a polymer nanocomposite via a hyperelastic double-continuous network of graphene and sponge. *Advanced functional materials*, 28(45):1805053, 2018.

[9] Yanming Xue, Xin Zhou, Tianzhuo Zhan, Baozhen Jiang, Quansheng Guo, Xiuwei Fu, Kiyoshi Shimamura, Yibin Xu, Takao Mori, Pengcheng Dai, et al. Densely interconnected porous bn frameworks for multifunctional and isotropically thermoconductive polymer composites. *Advanced Functional Materials*, 28(29):1801205, 2018.

[10] Weifei Wu, Tianli Ren, Xueqing Liu, Ryan Davis, Kai Huai, Xin Cui, Huaixiao Wei, Jinjin Hu, Yuming Xia, Shuohan Huang, et al. Creating thermal conductive pathways in polymer matrix by directional assembly of synergistic fillers assisted by electric fields. *Composites Communications*, 35:101309, 2022.

[11] Yang Xue, Haosheng Wang, Xiaofei Li, and Yunfa Chen. Exceptionally thermally conductive and electrical insulating multilaminar aligned silicone rubber flexible composites with highly oriented and dispersed filler network by mechanical shearing. *Composites Part A: Applied Science and Manufacturing*, 144:106336, 2021.

[12] Cuiping Yu, Wenbin Gong, Wei Tian, Qichong Zhang, Yancui Xu, Ziyin Lin, Ming Hu, Xiaodong Fan, and Yagang Yao. Hot-pressing induced alignment of boron nitride in polyurethane for composite films with thermal conductivity over 50 wm- 1 k- 1. *Composites Science and Technology*, 160:199–207, 2018.

[13] Yang Xue, Xiaofei Li, Haosheng Wang, Feng Zhao, Donghai Zhang, and Yunfa Chen. Improvement in thermal conductivity of through-plane aligned boron nitride/silicone rubber composites. *Materials & Design*, 165:107580, 2019.

[14] Chao Yuan, Bin Duan, Lan Li, Bin Xie, Mengyu Huang, and Xiaobing Luo. Thermal conductivity of polymer-based composites with magnetic aligned hexagonal boron nitride platelets. *ACS applied materials & interfaces*, 7(23):13000–13006, 2015.

[15] Kiho Kim and Jooheon Kim. Vertical filler alignment of boron nitride/epoxy composite for thermal conductivity enhancement via external magnetic field. *International Journal of Thermal Sciences*, 100:29–36, 2016.

[16] Minh Canh Vu, Won-Kook Choi, Sung Goo Lee, Pyeong Jun Park, Dae Hoon Kim, Md Akhtarul Islam, and Sung-Ryong Kim. High thermal conductivity enhancement of polymer composites with vertically aligned silicon carbide sheet scaffolds. *ACS applied materials & interfaces*, 12(20):23388–23398, 2020.

[17] Ravi Tutika, Shihuai H Zhou, Ralph E Napolitano, and Michael D Bartlett. Mechanical and functional tradeoffs in multiphase liquid metal, solid particle soft composites. *Advanced Functional Materials*, 28(45):1804336, 2018.

[18] Kun-Quan Ma and Jing Liu. Heat-driven liquid metal cooling device for the thermal management of a computer chip. *Journal of Physics D: Applied Physics*, 40(15):4722, 2007.

[19] Shengfu Mei, Yunxia Gao, Zhongshan Deng, and Jing Liu. Thermally conductive and highly electrically resistive grease through homogeneously dispersing liquid metal droplets inside methyl silicone oil. *Journal of Electronic Packaging*, 136(1):011009, 2014.

[20] Michael D Bartlett, Navid Kazem, Matthew J Powell-Palm, Xiaonan Huang, Wenhuan Sun, Jonathan A Malen, and Carmel Majidi. High thermal conductivity in soft elas-

tomers with elongated liquid metal inclusions. *Proceedings of the National Academy of Sciences*, 114(9):2143–2148, 2017.

[21] Xiaohong Wang, Chennan Lu, and Wei Rao. Liquid metal-based thermal interface materials with a high thermal conductivity for electronic cooling and bioheat-transfer applications. *Applied Thermal Engineering*, 192:116937, 2021.

[22] Ethan J Krings, Haipeng Zhang, Suchit Sarin, Jeffery E Shield, Sangjin Ryu, and Eric J Markvicka. Lightweight, thermally conductive liquid metal elastomer composite with independently controllable thermal conductivity and density. *Small*, 17(52):2104762, 2021.

[23] Phillip Won, Connor S Valentine, Mason Zadan, Chengfeng Pan, Michael Vinciguerra, Dinesh K Patel, Seung Hwan Ko, Lynn M Walker, and Carmel Majidi. 3d printing of liquid metal embedded elastomers for soft thermal and electrical materials. *ACS Applied Materials & Interfaces*, 14(49):55028–55038, 2022.

[24] Michael D Dickey. Emerging applications of liquid metals featuring surface oxides. *ACS applied materials & interfaces*, 6(21):18369–18379, 2014.

[25] MAH Khondoker and Dan Sameoto. Fabrication methods and applications of microstructured gallium based liquid metal alloys. *Smart Materials and Structures*, 25(9):093001, 2016.

[26] Sen Chen, Ruiqi Zhao, Xuyang Sun, Hongzhang Wang, Lei Li, and Jing Liu. Toxicity and biocompatibility of liquid metals. *Advanced Healthcare Materials*, 12(3):2201924, 2023.

[27] Michael D Dickey. Stretchable and soft electronics using liquid metals. *Advanced materials*, 29(27):1606425, 2017.

[28] Ravi Tutika, ABM Tahidul Haque, and Michael D Bartlett. Self-healing liquid metal composite for reconfigurable and recyclable soft electronics. *Communications Materials*, 2(1):64, 2021.

[29] Ethan J Krings, Benjamin D Hage, Sequoia L Truong, Kiersten A Reeser, Eli L Fox, Matthew G Snyder, Quentin Walker, Gregory R Bashford, and Eric J Markvicka. Acoustic properties of stretchable liquid metal-elastomer composites for matching layers in wearable ultrasonic transducer arrays. *Advanced Functional Materials*, page 2308954, 2023.

[30] Mohammad H Malakooti, Navid Kazem, Jiajun Yan, Chengfeng Pan, Eric J Markvicka, Krzysztof Matyjaszewski, and Carmel Majidi. Liquid metal supercooling for low-temperature thermoelectric wearables. *Advanced functional materials*, 29(45):1906098, 2019.

[31] Ren-Mian Chin, Youngshang Han, and Mohammad H Malakooti. Surface-engineered liquid metal particles for printing stretchable conductive composites with enhanced stability under different strain rates. *Advanced Materials Technologies*, 9(14):2301324, 2024.

[32] Michael J Ford, Dinesh K Patel, Chengfeng Pan, Sarah Bergbreiter, and Carmel Majidi. Controlled assembly of liquid metal inclusions as a general approach for multifunctional composites. *Advanced Materials*, 32(46):2002929, 2020.

[33] Dong Hae Ho, Chenhao Hu, Ling Li, and Michael D Bartlett. Soft electronic vias and interconnects through rapid three-dimensional assembly of liquid metal microdroplets. *Nature Electronics*, pages 1–10, 2024.

[34] Xuelin Wang, Rui Guo, and Jing Liu. Liquid metal based soft robotics: materials, designs, and applications. *Advanced Materials Technologies*, 4(2):1800549, 2019.

[35] Limeng Zheng, Stephan Handschuh-Wang, Zhicheng Ye, and Ben Wang. Liquid metal droplets enabled soft robots. *Applied Materials Today*, 27:101423, 2022.

[36] Eric J Markvicka, Michael D Bartlett, Xiaonan Huang, and Carmel Majidi. An autonomously electrically self-healing liquid metal–elastomer composite for robust soft-matter robotics and electronics. *Nature materials*, 17(7):618–624, 2018.

[37] Yoon Young Choi, Dong Hae Ho, and Jeong Ho Cho. Self-healable hydrogel–liquid metal composite platform enabled by a 3d printed stamp for a multimodular sensor system. *ACS applied materials & interfaces*, 12(8):9824–9832, 2020.

[38] Osman Gul, Kyuyoung Kim, Jimin Gu, Jungrak Choi, Dionisio Del Orbe Henriquez, Junseong Ahn, and Inkyu Park. Sensitivity-controllable liquid-metal-based pressure sensor for wearable applications. *ACS Applied Electronic Materials*, 3(9):4027–4036, 2021.

[39] Kyuyoung Kim, Junseong Ahn, Yongrok Jeong, Jungrak Choi, Osman Gul, and Inkyu Park. All-soft multiaxial force sensor based on liquid metal for electronic skin. *Micro and Nano Systems Letters*, 9:1–8, 2021.

[40] Kyuyoung Kim, Jungrak Choi, Yongrok Jeong, Incheol Cho, Minseong Kim, Seunghwan Kim, Yongsuk Oh, and Inkyu Park. Highly sensitive and wearable liquid metal-based pressure sensor for health monitoring applications: integration of a 3d-printed microbump array with the microchannel. *Advanced healthcare materials*, 8(22):1900978, 2019.

[41] El Mehdi Abbara, Mohammed Alhendi, Riadh Al-haidari, Nathaniel Gee, Mark D Poliks, Emily Boggs, Tan Yewteck, Deepak Trivedi, Christopher E Tabor, et al. Electromechanical and thermal characterization of printed liquid metal ink on stretchable substrate for soft robotics multi-sensing applications. In *2023 IEEE 73rd Electronic Components and Technology Conference (ECTC)*, pages 426–431. IEEE, 2023.

[42] Spencer Pak, Michael D. Bartlett, and Eric J. Markvicka. Direct ink write 3d printing of fully dense and functionally graded liquid metal elastomer foams. *Advanced Functional Materials*, page 202410908, 2024.

[43] ABM Tahidul Haque, Ravi Tutika, Rachael L Byrum, and Michael D Bartlett. Programmable liquid metal microstructures for multifunctional soft thermal composites. *Advanced Functional Materials*, 30(25):2000832, 2020.

[44] Jacob Mingear, Zachary Farrell, Darren Hartl, and Christopher Tabor. Gallium–indium nanoparticles as phase change material additives for tunable thermal fluids. *Nanoscale*, 13(2):730–738, 2021.

[45] Tyler A Pozarycki, Wuzhou Zu, Brittan T Wilcox, and Michael D Bartlett. A flexible and electrically conductive liquid metal adhesive for hybrid electronic integration. *Advanced Functional Materials*, page 2313567, 2024.

[46] Amanda Koh, Jennifer Sietins, Geoffrey Slipher, and Randy Mrozek. Deformable liquid metal polymer composites with tunable electronic and mechanical properties. *Journal of Materials Research*, 33(17):2443–2453, 2018.

[47] Ravi Tutika, Steven Kmiec, ABM Tahidul Haque, Steve W Martin, and Michael D Bartlett. Liquid metal–elastomer soft composites with independently controllable and highly tunable droplet size and volume loading. *ACS applied materials & interfaces*, 11(19):17873–17883, 2019.

[48] Chengfeng Pan, Eric J Markvicka, Mohammad H Malakooti, Jiajun Yan, Leiming Hu, Krzysztof Matyjaszewski, and Carmel Majidi. A liquid-metal–elastomer nanocomposite for stretchable dielectric materials. *Advanced Materials*, 31(23):1900663, 2019.

[49] Seoyeon Kim, Sihyun Kim, Kyeongmin Hong, Michael D Dickey, and Sungjune Park. Liquid-metal-coated magnetic particles toward writable, nonwettable, stretchable cir-

cuit boards, and directly assembled liquid metal-elastomer conductors. *ACS Applied Materials & Interfaces*, 14(32):37110–37119, 2022.

[50] Ruiqi Zhu, Zhenyang Li, Gao Deng, Yuanhang Yu, Jianglan Shui, Ronghai Yu, Caofeng Pan, and Xiaofang Liu. Anisotropic magnetic liquid metal film for wearable wireless electromagnetic sensing and smart electromagnetic interference shielding. *Nano Energy*, 92:106700, 2022.

[51] Guolin Yun, Shi-Yang Tang, Qianbin Zhao, Yuxin Zhang, Hongda Lu, Dan Yuan, Shuaishuai Sun, Lei Deng, Michael D Dickey, and Weihua Li. Liquid metal composites with anisotropic and unconventional piezoconductivity. *Matter*, 3(3):824–841, 2020.

[52] Shen Chen, Wenkui Xing, Han Wang, Weizheng Cheng, Zhihui Lei, Feiyu Zheng, Peng Tao, Wen Shang, Benwei Fu, Chengyi Song, et al. A bottom-up approach to generate isotropic liquid metal network in polymer-enabled 3d thermal management. *Chemical Engineering Journal*, 439:135674, 2022.

[53] David B Kolesky, Ryan L Truby, A Sydney Gladman, Travis A Busbee, Kimberly A Homan, and Jennifer A Lewis. 3d bioprinting of vascularized, heterogeneous cell-laden tissue constructs. *Advanced materials*, 26(19):3124–3130, 2014.

[54] Arda Kotikian, Ryan L Truby, John William Boley, Timothy J White, and Jennifer A Lewis. 3d printing of liquid crystal elastomeric actuators with spatially programed nematic order. *Advanced materials*, 30(10):1706164, 2018.

[55] Daniel J Braconnier, Robert E Jensen, and Amy M Peterson. Processing parameter correlations in material extrusion additive manufacturing. *Additive Manufacturing*, 31:100924, 2020.

[56] Tahamina Nasrin, Masoumeh Pourali, Farhad Pourkamali-Anaraki, and Amy M Peterson. Active learning for prediction of tensile properties for material extrusion additive manufacturing. *Scientific Reports*, 13(1):11460, 2023.

[57] Lawrence T Smith and Robert B MacCurdy. Digital multiphase composites via additive manufacturing. *Advanced Materials*, page 2308491, 2024.

[58] Lawrence Smith, Brandon Hayes, Kurtis Ford, Elizabeth Smith, David Flores, and Robert MacCurdy. Tunable metamaterials for impact mitigation. *Advanced Materials Technologies*, 9(6):2301668, 2024.

[59] Aaron Haake, Ravi Tutika, Gwyneth M Schloer, Michael D Bartlett, and Eric J Markvicka. On-demand programming of liquid metal-composite microstructures through direct ink write 3d printing. *Advanced Materials*, 34(20):2200182, 2022.

[60] Ohnyoung Hur, Ravi Tutika, Neal Klemba, Eric J Markvicka, and Michael D Bartlett. Designing liquid metal microstructures through directed material extrusion additive manufacturing. *Additive Manufacturing*, page 103925, 2023.

[61] Wuzhou Zu, Hugo E Carranza, and Michael D Bartlett. Enhancing electrical conductivity of stretchable liquid metal–silver composites through direct ink writing. *ACS Applied Materials & Interfaces*, 2024.

[62] Von DAG Bruggeman. Berechnung verschiedener physikalischer konstanten von heterogenen substanzen. i. dielektrizitätskonstanten und leitfähigkeiten der mischkörper aus isotropen substanzen. *Annalen der physik*, 416(7):636–664, 1935.

[63] Ian D Tevis, Lucas B Newcomb, and Martin Thuo. Synthesis of liquid core–shell particles and solid patchy multicomponent particles by shearing liquids into complex particles (slice). *Langmuir*, 30(47):14308–14313, 2014.

[64] T Ohmura, M Tsuboi, and T Tomimura. Estimation of the mean thermal conductivity of anisotropic materials. *International Journal of Thermophysics*, 23:843–853, 2002.

[65] T Borca-Tasciuc, AR Kumar, and G Chen. Data reduction in 3ω method for thin-film thermal conductivity determination. *Review of scientific instruments*, 72(4):2139–2147, 2001.

[66] ASTM D7984-16. Standard test method for measurement of thermal effusivity of fabrics using a modified transient plane source (mtps) instrument, 2016.